

# Propagation in Layered Biased Semiconductor Structures Based on Transport Analysis

CLIFFORD M. KROWNE, SENIOR MEMBER, IEEE, AND GREGORY B. TAIT, STUDENT MEMBER, IEEE

**Abstract**—A transport-field parallel-plate formulation and solution method to determine the small-signal propagation constant is given for wide microstrip lines over an inhomogeneously doped semiconductor substrate of small transverse dimensions. Included in the detailed transport model are two carrier species, recombination-generation mechanisms, dc and ac field-dependent mobilities and diffusion constants, and boundary condition contact effects. A transverse dc bias condition is applied. Structures numerically simulated are a voltage-variable GaAs distributed Schottky barrier phase shifter and a transmission line over a Si bipolar junction. Numerical data based on a finite difference technique are generated on carrier densities, electric potentials and fields, and current densities. Propagation constant calculations were favorably compared with those calculated by both full-wave field analysis and moments-of-the-Boltzmann-equation analysis for some less general cases.  $\gamma$  results for the GaAs structure are compared with available experimental data.

## I. INTRODUCTION

WAVEGUIDING structures loaded with extrinsic semiconductor material are utilized in both monolithic microwave integrated circuits (MMIC's) and high-speed digital large scale integrated (LSI) and very large scale integrated (VLSI) circuits. Distributed FET and IMPATT amplifiers, voltage-variable phase shifters, and tunable attenuators are several examples of distributed MMIC devices which employ the interaction of the charge carriers with the electromagnetic fields in semiconductors [1]–[4]. Also, microstrip and coplanar transmission lines over layered semiconductor media are used for interconnections between active devices in MMIC and VLSI technologies. The interconnections generally lie over passive semiconductor material, except in the vicinity of active devices where a transition region exists.

Analysis of metal–insulator–semiconductor (MIS) transmission lines and distributed Schottky contact lines has been carried out in the past with field approaches utilizing a single constant conductivity to model each doped semiconductor layer [5]–[9]. These field approaches, which range in complexity from quasi-TEM to full-wave analyses, have been successful in predicting the performance of MIS structures and uniformly doped, biased Schottky structures. This success is due to the lack of transverse currents because of a distinct insulator–semiconductor interface (MIS structures) and uniform conductivities in

individual semiconductor bulk layers (MIS and Schottky structures). When the semiconductor volume contains several junctions (such as  $pn$  and  $n^+n$ ) or intentionally graded doped areas, the constant-conductivity assumption no longer always represents the transverse transport accurately.

For example, diffusion of carriers away from the transitional zones between bulk and space-charge depletion regions in the vicinity of a junction causes a change in the field-carrier interaction within a few Debye lengths of each regional interface. Static dc characteristics as well as ac characteristics of the transport behavior will be altered. As a result, wave propagation behavior will also be changed. These additional considerations are especially important for structures which have very small transverse dimensions, such as micron and submicron feature sizes, which are increasingly seen in higher frequency (millimeter wave), higher speed (GHz digital and logic pulse), or denser circuits.

In this paper a transport-field parallel-plate formulation and solution method to find the small-signal propagation constant  $\gamma$  is presented for wide microstrip lines (with respect to transverse dimensions) over an inhomogeneously doped semiconductor substrate. The formulation approach includes dual carrier transport (electrons and holes); recombination-generation mechanisms (direct band gap, Shockley–Read–Hall, and Auger); dc and ac field-dependent carrier mobilities ( $\mu_n(E)$ ,  $\mu_p(E)$ ,  $\mu_{na}(E)$ , and  $\mu_{pa}(E)$ ); field-dependent diffusion constants ( $D_n(E)$  and  $D_p(E)$ ); and boundary condition contact effects at the guiding structure walls (ohmic and Schottky contacts). The  $E$ -field dependence of mobility is important since it allows negative differential conductivity to occur in some regions of a structure possessing a III–V semiconductor material.

The theoretical approach contained herein avoids the aforementioned difficulties when a field-transport model possessing an oversimplified transport description of the carriers is used. Section II covers the construction of the field-transport model of the microstrip structure. A simultaneous set of coupled ac equations are obtained which describe  $TM_z$  electromagnetic propagation. The method yields the dominant mode propagation constant  $\gamma$  for the strip over passive or active semiconductor substrates and retains dispersion through a detailed transport model. Section III discusses the numerical finite difference technique

Manuscript received February 16, 1988; revised October 26, 1988.

The authors are with the Electronics Science and Technology Division, Naval Research Laboratory, Washington, DC 20375-5000.

IEEE Log Number 8826041.

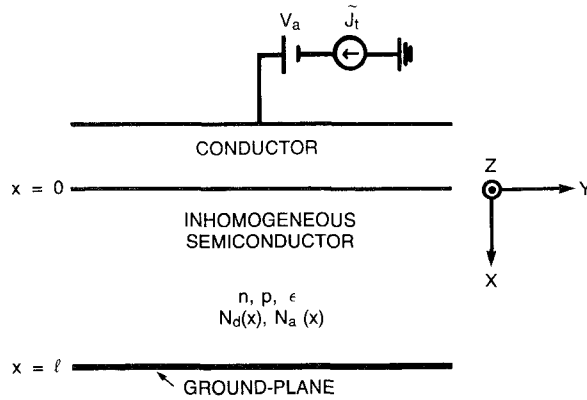


Fig. 1. Cross-sectional sketch of propagation structure. Microstrip conductor lies on top of an inhomogeneous semiconductor. Bias consists of applied dc voltage  $V_a$  and ac current  $\tilde{J}_t$ .

and boundary conditions applied toward solving the large number of simultaneous sets of dc and ac equations. Section IV presents numerical results for two demonstrative structures and provides comparison to some experimental data. The structures are a voltage-variable phase shifter employing a distributed microstrip Schottky contact on an n-GaAs semiconductor substrate and a microstrip-like transmission line over an active bipolar junction in Si. The approach presented here may be appropriate for characterizing propagation properties of gate, source, and drain lines in large-width MESFET and JFET devices at microwave frequencies where the characteristic lengths exceed the epitaxial layer thickness [3], [9].

## II. FIELD-TRANSPORT FORMULATION

Small-signal perturbations of the variables are assumed. For an arbitrary variable  $\nu(\mathbf{r}, t)$ ,

$$\nu(\mathbf{r}, t) = \nu_0(\mathbf{r}) + \tilde{\nu}(\mathbf{r}) e^{j\omega t - \gamma z} \quad (1)$$

the sum of a dc term and an ac term with a propagation constant  $\gamma$  ( $\nu$  may be a vector). Applying the parallel-plate assumption that the strip widths are large,  $\partial/\partial y$  terms in the analysis to follow are dropped. Fig. 1 shows the geometry of the structure in cross section. The effects of the conductor on the propagation behavior are accounted for by an ohmic or Schottky boundary condition (BC, whichever is appropriate) and an independently calculated attenuation constant  $\alpha_c$  based upon the skin effect. This surface lies on the semiconductor, which may possess an arbitrary doping profile of donors  $N_d(x)$  and acceptors  $N_a(x)$ , leading to a two-carrier transport system. Thus the electron  $n$  and hole  $p$  concentrations can be constant, rapidly varying, or lead to junction areas where space-charge depletion regions exist.

In the semiconductor volume the carriers and field obey the current continuity relations [10], [11]

$$\frac{\partial n}{\partial t} = \frac{1}{q} \nabla \cdot \mathbf{J}_n - R_n(n, p) \quad (2a)$$

$$\frac{\partial p}{\partial t} = -\frac{1}{q} \nabla \cdot \mathbf{J}_p - R_p(n, p) \quad (2b)$$

where  $\mathbf{J}_n$ ,  $\mathbf{J}_p$ ,  $R_n$ ,  $R_p$ , and  $q$  are, respectively, the particle

electron and hole current density vectors, the electron and hole net recombination rates, and the electronic charge magnitude.  $R_n = R_p = R$  is specified to avoid a net sink (or source) of charge (subtract (2b) from (2a) to see this point). A local field representation is used for  $\mathbf{J}_n$  and  $\mathbf{J}_p$ :

$$\mathbf{J}_n = -qnv_n + qD_n \nabla n \quad (3a)$$

$$\mathbf{J}_p = qpv_p - qD_p \nabla p \quad (3b)$$

$$\mathbf{v}_n = -\mu_n \mathbf{E} \quad (3c)$$

$$\mathbf{v}_p = \mu_p \mathbf{E}. \quad (3d)$$

Here the electron and hole mobilities and diffusion constants are, respectively,  $\mu_n$ ,  $\mu_p$ ,  $D_n$ , and  $D_p$ , which depend upon the local electric field  $\mathbf{E}$ . The total particle current density is

$$\mathbf{J} = \mathbf{J}_n + \mathbf{J}_p. \quad (4)$$

By setting  $E_y = E_z = 0$  and  $J_y = J_z = 0$ ,  $y$ - and  $z$ -directed currents are avoided in the analysis. Thus the problem is reduced to one of determining the propagation constant  $\gamma$  for the dominant  $TM_z$  mode as seen by invoking Faraday's law and employing the procedure below. (The situation of nonzero  $J_y$  and  $J_z$  and its creation of higher order  $TM_z$  modes or hybrid modes are discussed in Appendix I.)

Using Poisson's equation ( $\epsilon$  is the dielectric constant)

$$\nabla \cdot \mathbf{E} = \frac{q}{\epsilon} (p - n + N_d - N_a) \quad (5)$$

two sets of zeroth-order (dc case) and first-order (ac case) equations are obtained by placing (1) into (2), (3), and (5). Restricting the solution to a small differential cell in the  $z$  direction ( $\gamma = 0$ ), the dc case yields

$$\frac{dE_{x0}}{dx} = \frac{q}{\epsilon} (p_0 - n_0 + N_d - N_a) \quad (6a)$$

$$\frac{dJ_{n0x}}{dx} = qR_{dc}(n_0, p_0) \quad (6b)$$

$$\frac{dJ_{p0x}}{dx} = -qR_{dc}(n_0, p_0) \quad (6c)$$

$$J_{n0x} = q\mu_n(E_{x0})n_0E_{x0} + qD_n(E_{x0})\frac{dn_0}{dx} \quad (6d)$$

$$J_{p0x} = q\mu_p(E_{x0})p_0E_{x0} - qD_p(E_{x0})\frac{dp_0}{dx} \quad (6e)$$

and the ac case yields

$$\frac{d\tilde{J}_{nx}}{dx} = j\omega q\tilde{n} + qR_{ac}(\tilde{n}, \tilde{p}; n_0, p_0) \quad (7a)$$

$$\frac{d\tilde{J}_{px}}{dx} = -j\omega q\tilde{p} - qR_{ac}(\tilde{n}, \tilde{p}; n_0, p_0) \quad (7b)$$

$$\begin{aligned} \frac{d\tilde{n}}{dx} &= \frac{1}{qD_n} \left[ 1 + \frac{q\mu_{nax}n_0}{j\omega\epsilon} \right] \tilde{J}_{nx} \\ &\quad - \frac{\mu_{nax}n_0}{j\omega\epsilon D_n} (\tilde{J}_t - \tilde{J}_{px}) - \frac{\mu_n}{D_n} E_{x0} \tilde{n} \end{aligned} \quad (7c)$$

$$\begin{aligned} \frac{d\tilde{p}}{dx} &= -\frac{1}{qD_p} \left[ 1 + \frac{q\mu_{pax}p_0}{j\omega\epsilon} \right] \tilde{J}_{px} \\ &\quad + \frac{\mu_{pax}p_0}{j\omega\epsilon D_p} (\tilde{J}_t - \tilde{J}_{nx}) + \frac{\mu_p}{D_p} E_{x0} \tilde{p}. \end{aligned} \quad (7d)$$

Here  $\mu_{nax, pax} \equiv d\psi_{nx, px}(E_{x0})/dE_x$ , where  $E$  is the total electric field magnitude.  $\tilde{J}_t$  is the total ac terminal current density. Using the dc equations (6) subject to satisfactory BC,  $n_0(x)$ ,  $p_0(x)$ , and  $E_{x0}(x)$  are known in (7). Equations (7) represent a simultaneous coupled system of four equations in four complex unknowns, or a coupled system of eight equations in eight unknown real and imaginary variables. All the other ac variables of interest can be found once the coupled (7) set is solved. The ac equations (7) are solved for a chosen  $\tilde{J}_t$ ,  $\tilde{E}_x$  determined through

$$\tilde{E}_x = (\tilde{J}_t - \tilde{J}_{px} - \tilde{J}_{nx})/(j\omega\epsilon) \quad (8)$$

and the propagation constant is determined as follows.

Differential cells which characterize transport in the  $x$  direction can subsequently be stacked in the  $z$  direction to obtain the propagation constant  $\gamma$ . This procedure [12] requires the calculation of an impedance based upon the transport. The two-terminal complex impedance  $Z$  ( $\Omega \cdot m^2$ , in the  $x$  direction) per unit area is found from

$$Z = \frac{\tilde{V}_a}{\tilde{J}_t}. \quad (9)$$

$Z$  is a small-signal impedance and does not depend upon  $\tilde{J}_t$ .  $\tilde{V}_a$  is the applied or resultant voltage (from the conductor strip to the ground plane under the semiconductor), given as

$$\tilde{V}_a = \int_0^l \tilde{E}_x dx. \quad (10)$$

The propagation is directly given as

$$\gamma = \sqrt{\frac{j\omega\mu l}{Z}}. \quad (11)$$

The correct sign for  $\gamma$  is selected based upon the required propagation direction.

The recombination rate  $R$  can be expressed as

$$R = \frac{pn - n_i^2}{\alpha(n, p)} \quad (12a)$$

where [10], [13], [14]

$$\alpha(n, p) = \begin{cases} c_0^{-1} \\ \tau_n(p + p_t) + \tau_p(n + n_t) \\ (c_n n + c_p p)^{-1}. \end{cases} \quad (12b)$$

$$(12c)$$

$$(12d)$$

The denominator  $\alpha(n, p)$  corresponds, respectively, to direct, Shockley–Read–Hall, or Auger recombination in (12);  $c_0$ ,  $c_n$ , and  $c_p$  are carrier capture rates for the direct and Auger processes. For illustration, the Shockley–Read–Hall recombination rate is used to specify  $R$ . For  $\alpha(n, p)$  in (12c),  $n_i$ ,  $\tau_n$ ,  $\tau_p$ ,  $n_t$ , and  $p_t$  are, respectively, defined as the intrinsic density, the electron and hole lifetimes for single level traps, and the electron and hole densities obtained by replacing the quasi-Fermi energies by the trap energy  $E_t$

(in the normal  $n$  and  $p$  Boltzmann expressions). Consequently,

$$R_{dc} = \frac{p_0 n_0 - n_i^2}{\tau_n(p_0 + p_t) + \tau_p(n_0 + n_t)} \quad (13a)$$

$$R_{ac} = \frac{n_0 \tilde{p} - p_0 \tilde{n}}{\tau_n(p_0 + p_t) + \tau_p(n_0 + n_t)} + \frac{(p_0 n_0 - n_i^2)(\tau_n \tilde{p} + \tau_p \tilde{n})}{[\tau_n(p_0 + p_t) + \tau_p(n_0 + n_t)]^2}. \quad (13b)$$

Here midgap traps with  $E_t = E_i$  (intrinsic Fermi energy) are used, and  $\tau_n$  and  $\tau_p$  variations with carrier densities are neglected.

For the unipolar n-GaAs material case,  $R = 0$  and  $\mu_n$  and  $D_n$  are related through the Einstein relationship,  $D_n = k_b T \mu_n / q$ .  $\mu_n$  was taken to be [15], [16]

$$\mu_n = [\mu_{n0} + \nu_{ns} E^3 / E_0^4] [1 + (E/E_0)^4]^{-1} \quad (14)$$

where  $\mu_{n0}$ ,  $\nu_{ns}$ , and  $E_0$  are, respectively, the low field mobility, the electron saturation velocity, and a reference electric field.  $\mu_{na}$  was calculated from (14) as

$$\mu_{na} \equiv \frac{d\nu_n}{dE} = \frac{d}{dE}(\mu_n E) = \mu_n [4 - 3\mu_{n0}/\mu_n] [1 + (E/E_0)^4]^{-1}. \quad (15)$$

GaAs parameters were set for a temperature of 300 K and a doping concentration  $N_{d0} = 10^{17} \text{ cm}^{-3}$  at  $\mu_{n0} = 5500 \text{ cm}^2/\text{V}\cdot\text{s}$ ,  $\nu_{ns} = 8.5 \times 10^6 \text{ cm/s}$ , and  $E_0 = 4.9 \text{ kV/cm}$  [15], [16]. Intrinsic density  $n_i$  and relative permittivity  $\epsilon_r$  were set at  $1.8 \times 10^6 \text{ cm}^{-3}$  and 13.1 respectively [11].

In the bipolar silicon material case,  $R \neq 0$ , and  $\mu_{n, p}$  is taken to be [14], [17]

$$\mu_{n, p} = \mu_{(n, p)0} [1 + \mu_{(n, p)0} E / v_{(n, p)s}]^{-1} \quad (16)$$

with the Einstein relationship utilized.  $\mu_{(n, p)a}$  were derived from (16) as

$$\mu_{(n, p)a} = \mu_{(n, p)}^2 / \mu_{(n, p)0}. \quad (17)$$

For a step junction in silicon, the parameters were set for 300 K temperature and doping concentrations  $N_{d0} = N_{a0} = 10^{17} \text{ cm}^{-3}$ , creating the doping profile

$$N(x) = N_d(x) - N_a(x) = N_{d0} u(x - l/2) - N_{a0} u(-x + l/2) \quad (18)$$

with  $t_n = 2.6 \times 10^{-5} \text{ s}$ ,  $\tau_p = 2.3 \times 10^{-6} \text{ s}$ ,  $\mu_{n0} = 825 \text{ cm}^2/\text{V}\cdot\text{s}$ ,  $\mu_{p0} = 340 \text{ cm}^2/\text{V}\cdot\text{s}$ ,  $\nu_{ns} = 1.0 \times 10^7 \text{ cm/s}$ , and  $v_{ps} = 9.5 \times 10^6 \text{ cm/s}$  [11], [14], [17]–[20]. In (18),  $l$  is the semiconductor thickness and  $u(x)$  is the unit step function.  $n_i$  and  $\epsilon_r$  were set at  $1.45 \times 10^{10} \text{ cm}^{-3}$  and 11.7 respectively [11].

### III. NUMERICAL APPROACH AND BOUNDARY CONDITIONS

The ac (or dc) transport equations (7) can be put into a convenient form for numerical solution by defining the normalizations [13], [21], [22]

$$\begin{aligned}\bar{E} &= \frac{qL_D}{k_b T} E & \bar{J} &= \frac{L_D}{qn_r D_0} J & \bar{\tau} &= \frac{D_0}{L_D^2} \tau & \bar{n} &= \frac{n}{n_r} \\ \bar{x} &= \frac{x}{L_D} & \bar{\omega} &= \frac{L_D^2}{D_0} \omega & \bar{D} &= \frac{D}{D_0} & \bar{\mu}_{na} &= \frac{k_b T}{qD_0} \mu_{na}\end{aligned}\quad (19)$$

where  $D_0$  is a constant and

$$L_D = \sqrt{\frac{\epsilon_s k_b T}{q^2 n_r}}$$

is an extrinsic Debye length based upon a chosen reference density  $n_r$  ( $k_b$  is Boltzmann's constant and  $T$  the temperature). For the n-GaAs material case  $D_0 = 3.0 \text{ cm}^2/\text{s}$  and  $n_r = 1.0 \times 10^{10} \text{ cm}^{-3}$  (dc),  $n_i$  (ac), and  $\tilde{J}_t$  was chosen to be  $5.6 \times 10^{-10} \text{ A/cm}^2$  (1 percent of the calculated metal-semiconductor junction dc reverse saturation current). In the Si material case,  $D_0 = 1.0 \text{ cm}^2/\text{s}$  and  $n_r = n_i$  (dc),  $1.0 \times 10^6 \text{ cm}^{-3}$  (ac), and  $\tilde{J}_t = 1.5 \times 10^{-11} \text{ A/cm}^2$  (1 percent of the calculated bipolar junction dc reverse saturation current).

Using the quasi-Fermi potential concept [10], [13], [23], [24], the electron and hole densities can be eliminated in the dc equations (6) with the substitutions

$$n_0 = n_i e^{q(\psi - \phi_n)/k_b T} \quad p_0 = n_i e^{q(\phi_p - \psi)/k_b T}. \quad (20)$$

Here  $\phi_p$  and  $\phi_n$  are, respectively, the hole and electron quasi-Fermi potentials and  $\psi$  is the electrostatic potential defined by

$$\frac{d\psi}{dx} = -E_{x0}. \quad (21)$$

The potential normalization used is

$$\bar{\psi} = \frac{q}{k_b T} \psi. \quad (22)$$

Boundary conditions need to be chosen for both the ac equations (7) and the dc equations (6) so that solutions can be sought for  $\gamma$ . Metal-semiconductor BC's are required at  $x = 0$  and  $x = l$ . For the dc case, Dirichlet BC's are specified for  $\bar{\psi}$  ( $= -E_t/K_b T$ ) and  $\bar{\phi}_n$  and  $\bar{\phi}_p$ . Thermal equilibrium [ $\bar{\phi}_n = \bar{\phi}_p$  in (20)] and charge neutrality [ $d\bar{E}_{x0}/d\bar{x} = 0$  in (6a)] are assumed when a contact is ohmic. Under these assumptions [10], [13]

$$\begin{aligned}\bar{\psi} &= \bar{V}_c + \ln \left[ \left( \bar{N} + (\bar{N}^2 + 4\bar{n}_i^2)^{1/2} \right) \right] / (2\bar{n}_i) \\ \bar{\phi}_n &= \bar{\phi}_p = \bar{V}_c\end{aligned}\quad (23)$$

for an ohmic contact. Here  $\bar{N}(x) = \bar{N}_d(x) - \bar{N}_a(x)$ .  $\bar{V}_c$  is the applied terminal potential at the contact, and is  $\bar{V}_a$  or 0 at, respectively,  $x = 0, l$ . When  $\bar{n}_i \ll \bar{N}$ , the logarithmic term in (23) is nearly  $\ln(\bar{N}/\bar{n}_i)$ . For  $\bar{N} < 0$  and  $\bar{n}_i \ll |\bar{N}|$ , the second term may be converted into a more convenient

form for numerical evaluation by multiplying the numerator and the denominator of the argument by  $\bar{N}$  minus the square root term (taken always to be the positive branch). When the contact forms a Schottky barrier,

$$\bar{\psi} = \bar{V}_c - \bar{\phi}_B + \bar{E}_g/2 \quad (24)$$

and  $\bar{\phi}_n = \bar{\phi}_p = \bar{V}_c$ . Equation (24) is based on an idealized Schottky contact. The difference between the conduction band edge and the intrinsic Fermi energy,  $E_c - E_i$ , is equated to half of the bandgap energy  $E_g$  (here normalized to  $k_b T$ ).  $\bar{\phi}_B$  is the normalized Schottky barrier voltage height, given by the difference  $\bar{\phi}_m - \bar{\chi}_s$  between the normalized metal work function and the electron affinity of the semiconductor [11]. Dirichlet BC's for the ac case are based on the assumed local equilibrium condition (fixed charge densities in time) of the carriers at the contacts. Perturbed ac variables  $\tilde{n}$  and  $\tilde{p}$  are, at  $x = 0, l$ ,

$$\tilde{n} = \tilde{p} = 0. \quad (25)$$

Boundary conditions (25), invoking (7a) and (7b), are equivalent to Neumann BC's on the current densities at  $x = 0, l$ :

$$\frac{d\bar{J}_{nx}}{d\bar{x}} = \frac{d\bar{J}_{px}}{d\bar{x}} = 0. \quad (26)$$

Systems of dc equations (6) and (21) and ac equations (7), subject to the BC's (23), (24), and (25), are solved on the NRL Cray X-MP/24 computer using the Cray Fortran programming language and an IMSL finite difference differential equation library subroutine [25], [26]. Since the IMSL subroutine necessitates the use of real variables, in actuality ac equations (7) constitute a system twice as large as listed. The finite difference approach utilizes trapezoidal rule discretizations over an adaptive nonuniform mesh, which provides for equidistribution of local truncation error. It is a variable high-order method relying upon the deferred correction technique. Enhanced convergence of the solution for the nonlinear dc system of equations is achieved through damped Newton iterations. The resulting linear system of equations has block quasi-tridiagonal matrices which are solved by LU decomposition with alternating partial pivoting. Computations proceed until the estimated relative error of each variable across the entire mesh in less than a specified relative error tolerance parameter  $\delta$ .

The choice of independent variables  $\bar{\psi}$ ,  $\bar{\phi}_n$ , and  $\bar{\phi}_p$  was made because they are all the same order of magnitude and typically do not change more than one order of magnitude across the whole structure. Therefore the accuracy of  $\bar{\psi}$ ,  $\bar{\phi}_n$ , and  $\bar{\phi}_p$  (and, accordingly,  $\bar{E}_{x0}$ ,  $\bar{J}_{n0x}$ ,  $\bar{J}_{p0x}$ ,  $\bar{n}_0$ , and  $\bar{p}_0$ ) across the mesh can be controlled precisely by  $\delta$ . Exponential nonlinearities in the dc equations pose no difficulties for the robust numerical method. For the linearized system of ac differential equations,  $n_r$  and  $D_0$  can be selected in conjunction with  $\tilde{J}_t$  and  $\delta$  to provide accurate values of the ac variables over many orders of magnitude. Judicious choices for  $n_r$ ,  $D_0$ ,  $\tilde{J}_t$ , and  $\delta$  are necessary to avoid  $\delta$  becoming an absolute error control parameter in the convergence criteria for a variable when it is below

unity, thereby possibly reducing accuracy. The IMSL subroutine recognizes linear differential equation systems and implements a very efficient algorithm. Required dc quantities are obtained by linear interpolation of stored dc values in common area arrays.

Good initial values (Appendix II) for the iterative Newton approach to converge are needed for the set of dc equations (6) and (21). First the equilibrium solution is found by entering values obtained from approximate analytical expressions (derived from the depletion approximation for junctions) over a selected nonuniform mesh. Nonequilibrium solutions are next found by incrementing the applied voltage (by  $\Delta\bar{V}_a$ ) and using the previous solution as input initial values. Following this procedure leads to rapid convergence for a solution at an applied voltage  $\bar{V}_a$ . For each successive bias voltage, the previous solution must be modified slightly to satisfy new BC's on  $\psi$ ,  $\phi_n$ , and  $\phi_p$  (see Appendix II).

Initial values for the ac variables are taken to be zero across the same final nonuniform mesh employed for the dc solution. Even for large ac terminal currents  $\tilde{J}_t$ , this prescription works well. Jacobian matrices which characterize the dc and ac differential equation systems are found by taking the partial derivatives of (6) (and (21)) and (7). These matrices are utilized by the IMSL DVCPR finite difference equation solving subroutine, and defined as  $\partial(d\bar{V}_i/d\bar{x})/\partial\bar{V}_j$ , where the indices  $i, j = 1, 2, \dots, M$  and  $\bar{V}_i$  is an unknown variable in the equation system.  $M$  is equal to the number of equations (or independent variables) in the system. For the dc system  $M = 6$  where all the dc variables are real quantities. The ac system has complex variables, and is numerically solved by breaking up each variable into its real and imaginary components. This decomposition creates an additional four ac equations so that  $M = 8$ . Typically, a single dc bias point is calculated in 1 to 8 s, depending upon the final number of mesh points. The maximum number of mesh points was set at 2000. A single ac frequency calculation usually took 1 to 4 s, again depending upon the final number of mesh points.

The accuracy of propagation constants  $\gamma$  determined from this computer solution of the ac set of equations was checked independently against those calculated from an analytical moments-of-Boltzmann-equation analysis [12] for a simple test case. In this test, spatially uniform dc variables and single carrier transport at a 300 K lattice temperature are assumed, and the  $\partial/\partial t$  and  $\partial(nv^2)/\partial x$  terms are dropped in the momentum balance equation [12, eq. (2)]. For the ac BC's (25) imposed on the perturbed carrier density,  $\gamma$  is given by (11), where

$$Z = \left( \frac{\tau_p q^2 n_0 l}{m^*} - j\omega\epsilon l \right) \left( \omega^2 \epsilon^2 + \frac{\tau_p^2 q^4 n_0^2}{m^{*2}} \right)^{-1}. \quad (27)$$

For a 3- $\mu\text{m}$ -long,  $10^{16} \text{ cm}^{-3}$  doped n-GaAs sample with  $\mu_n = 8500 \text{ cm}^2/\text{V}\cdot\text{s}$  ( $\tau_p = 3.29 \times 10^{-13} \text{ s}$ ) and  $f = 10 \text{ GHz}$ , (27) yields

$$Z = 2.20299 \times 10^{-5} - j1.15166 \times 10^{-7} \Omega \cdot \text{cm}^2$$

while the numerical ac code yields

$$Z = 2.20297 \times 10^{-5} - j1.15028 \times 10^{-7} \Omega \cdot \text{cm}^2.$$

From (11), it can be seen that both approaches give the same propagation constant in this test case,

$$\gamma = \alpha + j\beta = 73.1 + j73.5 \text{ cm}^{-1}.$$

#### IV. NUMERICAL RESULTS AND EXPERIMENTAL DATA

##### A. Schottky Transmission Line on n-GaAs

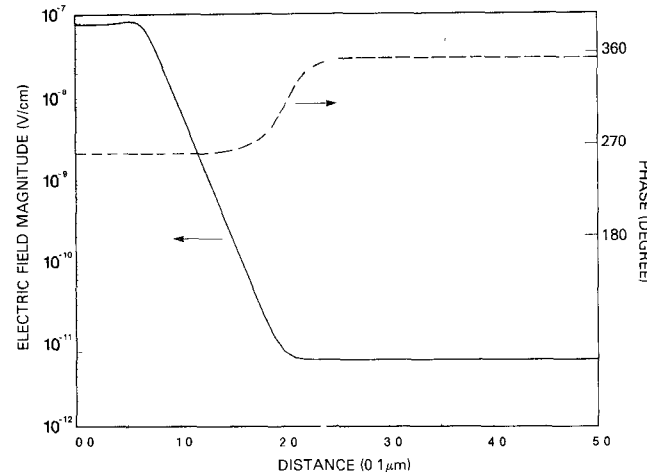
The first structure examined is a voltage-variable phase shifter employing a 1.5- $\mu\text{m}$ -wide, 1600- $\mu\text{m}$ -long Au/Pt/Ti Schottky transmission line on an n-GaAs epitaxial layer ( $N_{d0} = 10^{17} \text{ cm}^{-3}$ ,  $l = 2 \mu\text{m}$  thick) [1], [27]. Underneath this layer is an n<sup>+</sup>-GaAs epitaxial layer which is electrically accessed through large ohmic contact pads connected to ground over their full 1600  $\mu\text{m}$  length. This multilayered mesa structure is supported by a thick semi-insulating GaAs substrate. For the numerical calculations, the Schottky barrier height for Pt/Ti metallization on n-GaAs was taken to be  $\phi_B = 0.81 \text{ V}$  [28], and the n<sup>+</sup> layer was treated as the virtual ground plane.

The dc simulations were carried out over an applied voltage  $V_a$  range of  $-3.5 \text{ V}$  to  $+0.5 \text{ V}$ . The calculated dc electron particle currents were  $-5.6 \times 10^{-8} \text{ A/cm}^2$  and  $13.2 \text{ A/cm}^2$  for the  $-3.5 \text{ V}$  and  $+0.5 \text{ V}$  bias limits, respectively. The dc spatial profiles were then utilized in the ac simulations, which were run with impressed terminal currents operating at frequencies  $f$  from 1 GHz to 20 GHz. Fig. 2(a)–(c) shows the magnitudes and phase angles (with respect to the terminal current) for the ac electric field  $\tilde{E}_x$ , the electron current density  $\tilde{J}_{nx}$ , and the electron density  $\tilde{n}$  respectively for a dc bias  $V_a$  of  $+0.5 \text{ V}$  and a frequency of 1 GHz. Likewise, Fig. 3(a)–(c) shows the same ac quantities, but for a dc bias  $V_a$  of  $-3.5 \text{ V}$  and a frequency of 10 GHz.

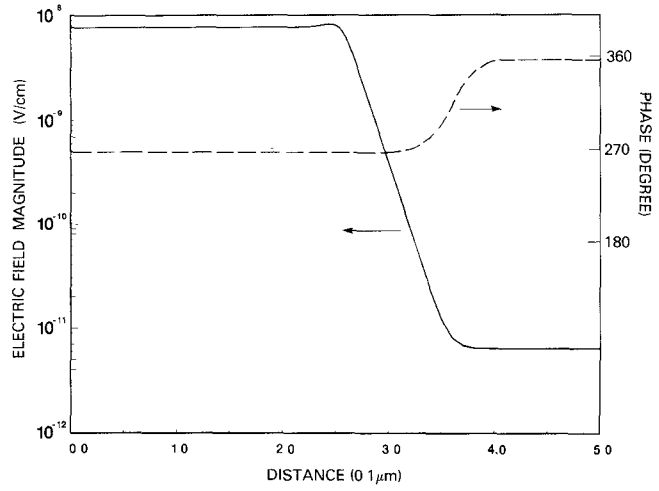
From these figures, it is evident that the width of the transition areas between space-charge depletion regions and bulk regions can be a large percentage of the depletion region width, and that these transition areas “penetrate” well into what would typically be categorized as the bulk region. In the  $V_a = +0.5 \text{ V}$  bias example, the transitional zone width for the ac electric field, Fig. 2(a), is nearly 100 percent of the depletion region width, and starts at approximately  $x \approx 0.06 \mu\text{m}$ , which is the edge of the depletion region as calculated from the analytical expression

$$x_d = \sqrt{2\epsilon(\phi_i - V_a)/(qN_{d0})}$$

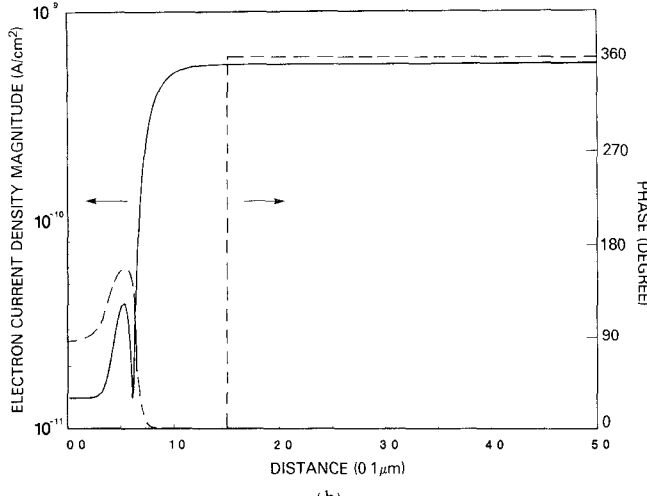
where  $\phi_i$  is the built-in potential. Similarly, the transitional area begins at approximately  $x = 0.25 \mu\text{m}$  (edge of analytically computed depletion region) and extends about 0.1  $\mu\text{m}$  further into the n layer for the  $V_a = -3.5 \text{ V}$  case (Fig. 3(a)). Unlike field solutions which assume a “hard,” distinct interface between the depletion region ( $\sigma = 0$ ) and the bulk region ( $\sigma = \text{constant}$ ), these “soft” transitions are more realistic and can be simulated only with a combined transport-field approach which can adequately describe



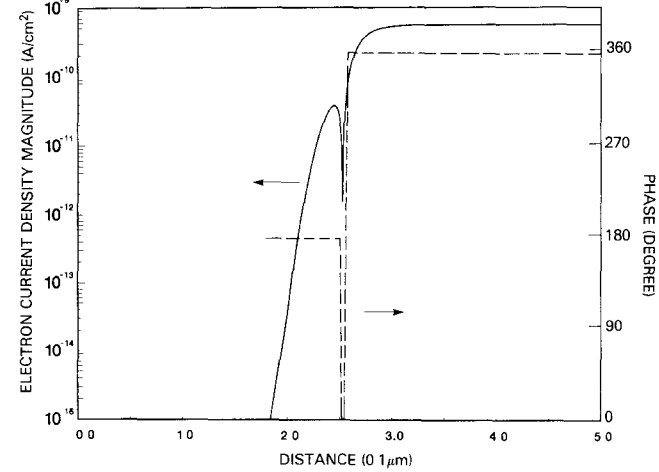
(a)



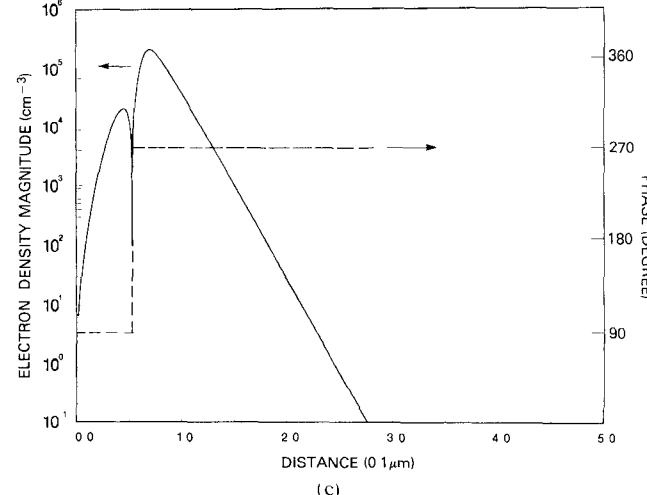
(a)



(b)

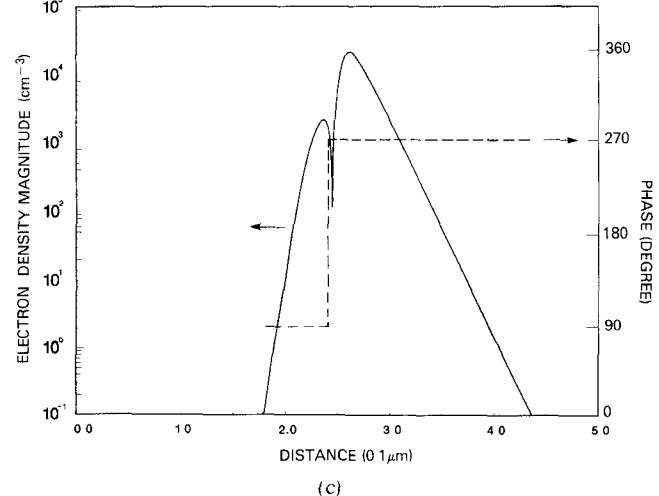


(b)



(c)

Fig. 2. GaAs Schottky line ac magnitude and phase spatial profiles of (a) electric field  $\tilde{E}_x$ , (b) electron current density  $\tilde{J}_{nx}$ , and (c) electron density  $\tilde{n}$  for  $V_a = +0.5$  V and ac frequency  $f$  of 1 GHz. Parameters are set at  $N_{d0} = 10^{17}$  cm $^{-3}$ ,  $\phi_B = 0.81$  V,  $l = 2 \mu\text{m}$ , and  $T = 300$  K. Abscissas show depth into GaAs from the distributed Schottky contact at  $x = 0$ .



(c)

Fig. 3. GaAs Schottky line ac magnitude and phase spatial profiles of (a) electric field  $\tilde{E}_x$ , (b) electron current density  $\tilde{J}_{nx}$ , and (c) electron density  $\tilde{n}$  for  $V_a = -3.5$  V and  $f = 10$  GHz. Parameters are the same as in Fig. 2.

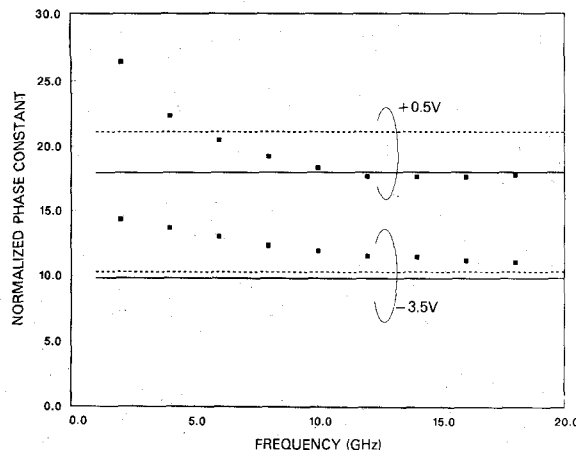


Fig. 4. GaAs Schottky line normalized phase constants  $\beta/\beta_0$  versus  $f$  for  $V_a = -3.5$  V and  $+0.5$  V. Transport-field analysis (—); full-wave field analysis (---); experimental data (□).

the transverse current characteristics. Furthermore, by allowing the electron mobility to vary with the electric field as shown in (14) and (15), negative differential conductance (NDC) effects may be present in regions of the structure where the electric field magnitude is on the order of the threshold field (approximately 4 kV/cm in GaAs). These field magnitudes occur in the transition areas. In fact, the magnitude "dips" and phase angle changes in the ac electron current density and electron density profiles (Figs. 2(b) and (c) and 3(b) and (c)) are caused by the GaAs mobility model which admits NDC. Monotonic mobility versus field curves, such as in Si, do not generate these NDC characteristics. If the NDC effect in these localized regions is strong enough, it is possible that the attenuation constant of the GaAs medium will be negative, thereby signifying distributed gain for the structure (see further discussion below). It is impossible to reproduce this gain result using a field solver which employs a single, positive-valued, constant conductivity for the transport description. Also, the transitions in the electric field and electron current density profiles (Figs. 2(a) and (b) and 3(a) and (b)) indicate the spatial transformation of a displacement-dominated current to a particle (electron) dominated current. For example, in the  $V_a = -3.5$  V bias case (Fig. 3(a) and (b)) the displacement current,  $j\omega\epsilon\tilde{E}_x \approx -\omega\epsilon\tilde{E}_{x,\text{imag}} \approx \tilde{J}_i$ , is dominant from  $x = 0$  to  $x \approx 0.25 \mu\text{m}$  (area largely depleted of mobile carriers), whereas the electron particle current,  $\tilde{J}_{nx,\text{real}} \approx qn_0\mu_n\tilde{E}_{x,\text{real}} \approx \tilde{J}_i$ , ( $\mu_n \approx \mu_{n0}$ ), becomes dominant beyond the transitional zone edge,  $x \gtrsim 0.35 \mu\text{m}$  (bulk region filled with carriers).

The wave propagation behavior may be obtained by calculating the complex propagation constant ( $\gamma = \alpha_s + j\beta$ ) for each ac frequency as in Section II. The results of these calculations are given in Figs. 4 and 5 and Table I, and are compared with a full-wave parallel-plate field-type solution method [6] (with  $l = 2 \mu\text{m}$ ,  $\sigma = 88.11 \text{ S/cm}$ ,  $N_{d0} = 10^{17} \text{ cm}^{-3}$ ,  $\phi_B = 0.81 \text{ V}$ ) and with experimental data [1], [27]. The depletion layer is represented by a perfect insulator in the full-wave analysis, and its thickness is determined from dc analytical equations (provided in Appendix II). Fig. 4 shows the normalized phase constants (or

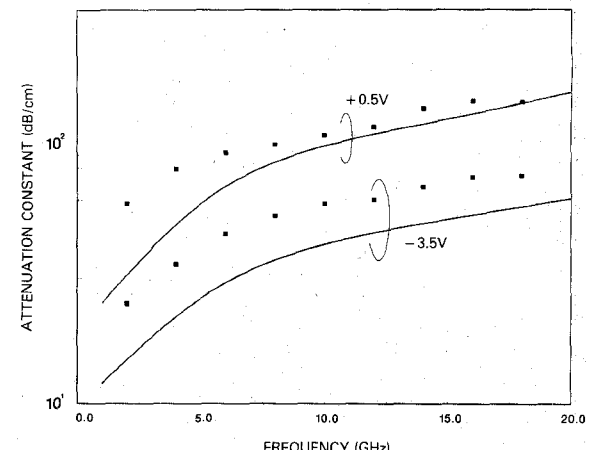


Fig. 5. GaAs Schottky line attenuation constants,  $\alpha$  (dB/cm), for  $V_a = -3.5$  V and  $+0.5$  V. Semiconductor transport-field and microstrip conductor analysis (—); experimental data (□).

TABLE I  
COMPARISON OF THEORETICAL TRANSPORT-FIELD VERSUS FULL-WAVE SEMICONDUCTOR ATTENUATION CONSTANTS,  $\alpha_s$  (db/cm), IN THE GAAS SCHOTTKY LINE EXAMPLE FOR TWO VALUES OF APPLIED DC BIAS VOLTAGE  $V_a$

F (GHz)	Attenuation Constant (dB/cm)			
	-3.5 V		+0.5 V	
	Transport	Full-Wave	Transport	Full-Wave
1	0.005	0.006	-0.379	0.054
5	0.116	0.151	0.384	1.352
10	0.464	0.606	2.768	5.406
15	1.044	1.363	6.741	12.15
20	1.855	2.422	12.30	21.58

Parameters are set at  $N_{d0} = 10^{17} \text{ cm}^{-3}$ ,  $\phi_B = 0.81 \text{ V}$ ,  $l = 2 \mu\text{m}$ , and  $T = 300 \text{ K}$ .

"slow-wave" factors)  $\beta/\beta_0 = c/v_p$ , where  $c$  and  $v_p$  are the speed of light in vacuum and the wave phase velocity, respectively, as a function of frequency for the two  $V_a$  cases. The two types of numerical calculations display no visible dispersive characteristics (less than 0.1 percent), but the transport-field  $\beta/\beta_0$  values are slightly smaller. This difference is consistent with the fact that the transitional areas predicted in the transport-field approach effectively increase the nominal depletion depth, and the phase constant is correspondingly smaller. On the other hand, the experimental  $\beta/\beta_0$  values show frequency dependence caused by field penetration into the virtual  $n^+$  epitaxial ground plane and substrate. The extent of this penetration is a function of the conductivity, the frequency, and the structural dimensions of these layers. Since the effective ground plane depth is greater than the  $n$  epitaxial layer thickness ( $2 \mu\text{m}$ ), the experimental  $\beta/\beta_0$  values are higher than the ones numerically calculated. Agreement, nevertheless, becomes very good at higher frequencies, as the effective ground plane depth decreases, and approaches  $2 \mu\text{m}$ .

The GaAs losses predicted from the numerically obtained attenuation constants  $\alpha_s$  are shown in Table I for the  $1600\text{-}\mu\text{m}$ -long structure. For the  $V_a = -3.5$  V case, the losses are small due to the mostly nonlossy "dielectric" nature of the relatively wide depletion width. Material

losses in the  $V_a = +0.5$  V case are larger for frequencies greater than 5 GHz since the depletion width is extremely narrow. For frequencies less than 5 GHz, however, NDC characteristics of the Schottky microstrip structure with applied bias of  $V_a = +0.5$  V are simulated by the transport-field method, and a very small gain is predicted. Actually, the total attenuation constant for the structure,  $\alpha = \alpha_s + \alpha_c$ , is dominated by ohmic loss in the metallic microstrip conductor ( $\alpha_c$ ), and this loss mechanism swamps out any gain contribution from the GaAs semiconductor material (negative  $\alpha_s$ ). In order to estimate this conductor loss, a microstrip computer program was utilized with the experimental  $\beta/\beta_0$  values providing the effective permittivity values ( $\epsilon_{\text{eff}}$ ) and effective ground plane spacings ( $b_{\text{eff}}$ ) as follows [1]:

$$\epsilon_{\text{eff}} = (\beta/\beta_0)^2 \quad (28a)$$

and

$$b_{\text{eff}} (\text{cm}) = (\epsilon_{\text{eff}}/\epsilon) \sqrt{2\epsilon(\phi_i - V_a)/(qN_{d0})}. \quad (28b)$$

The thickness  $t$  of the microstrip line is 0.63  $\mu\text{m}$ . The Au/Pt/Ti microstrip resistivity is taken as  $\rho_{\text{Au}} = 2.44 \times 10^{-6} \Omega \cdot \text{cm}$ .  $\alpha_c$  (dB/cm) is calculated by a standard method [29]. The sum of the theoretically calculated semiconductor and metal contributions to the loss is plotted against the actual experimental loss data in Fig. 5 for the two  $V_a$  cases. In these comparisons, the calculated loss values are smaller than the experimental ones, since the numerical simulation accounted for neither field penetration into the virtual  $n^+$  epitaxial ground plane and substrate nor other sources of experimental loss. The same frequency behavior, however, is observed. At lower frequencies, the approximate  $\sqrt{f}$  behavior due to the metallic conduction mechanism of the strip is evident, but the semiconductor losses are seen to contribute as well at the higher frequencies, where the loss increases with frequency at a rate somewhat higher than  $\sqrt{f}$ .

### B. Transmission Line over Si Bipolar Junction

The next structure examined is a transmission line interconnect over a Si bipolar step junction with a very small transverse dimension (3  $\mu\text{m}$ ). Although interconnections generally lie over passive semiconductor material, they must also pass in the vicinity of, or sometimes over, active devices which have micron and submicron feature sizes for higher speed (GHz digital and logic pulse) and denser circuits. The wave propagation behavior through these active, inhomogeneously doped semiconductor regions is determined by considering the two-carrier (electron and hole) transport interaction with the electromagnetic field.

The dc simulations were carried out over an applied voltage  $V_a$  range of  $-3.0$  V to  $+0.3$  V. (The metallurgical junction is located at  $x = 0$ , and distances of 0.4  $\mu\text{m}$  are shown in the figures below on both sides of this junction.) Minority carrier current densities  $J_{n0x}$  and  $J_{p0x}$  in, respectively, the left- and right-hand sides of the semiconductor

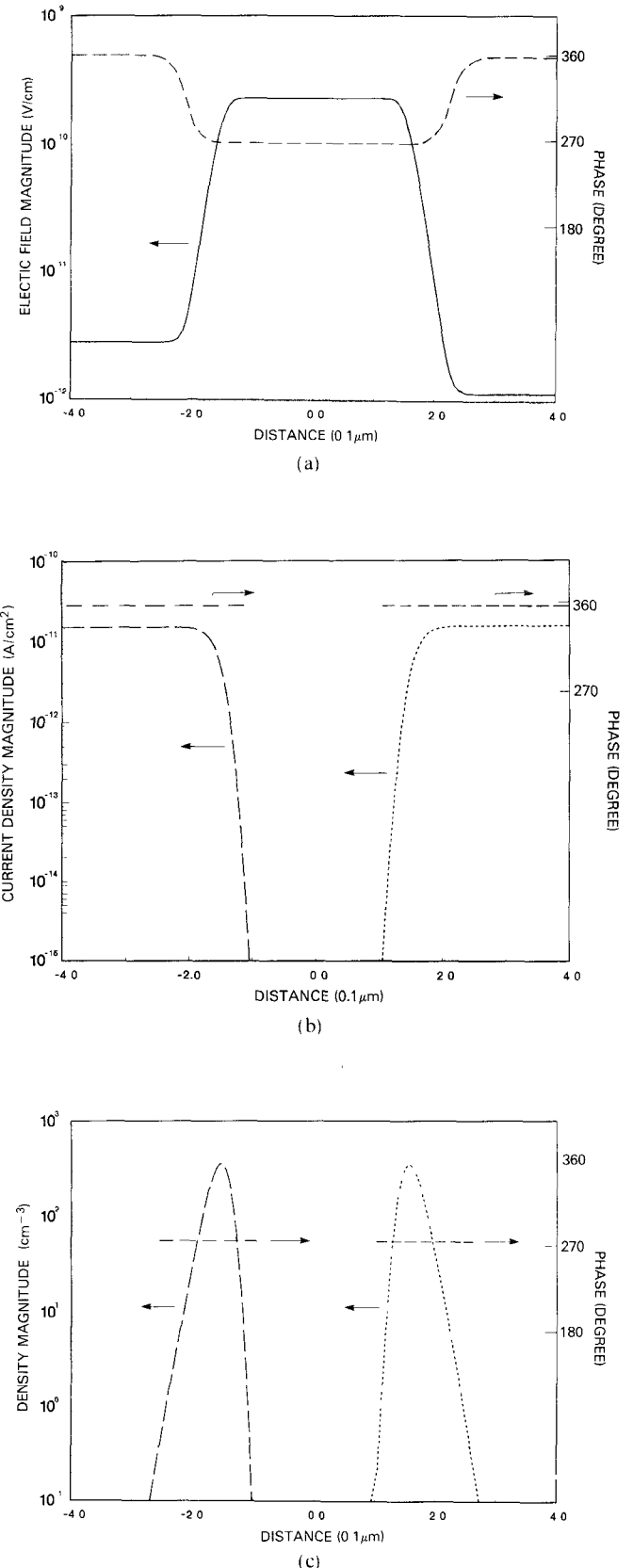


Fig. 6. Si transmission line ac magnitude and phase spatial profiles of (a) electric field  $\tilde{E}_x$ , (b) electron  $\tilde{J}_{n\gamma}$  (----) and hole  $\tilde{J}_{p\gamma}$  (—·—·) current densities, and (c) electron  $\tilde{n}$  (----) and hole  $\tilde{p}$  (—·—·) densities for  $V_a = -3.0$  V and  $f = 10$  GHz. Parameters are set at  $N_{d0} = N_{a0} = 10^{17} \text{ cm}^{-3}$  and  $T = 300$  K. The metallurgical junction is located at  $x = 0$ , and the distributed ohmic contact and the ground plane are located at  $x = -1.5 \mu\text{m}$  and  $x = 1.5 \mu\text{m}$ , respectively.

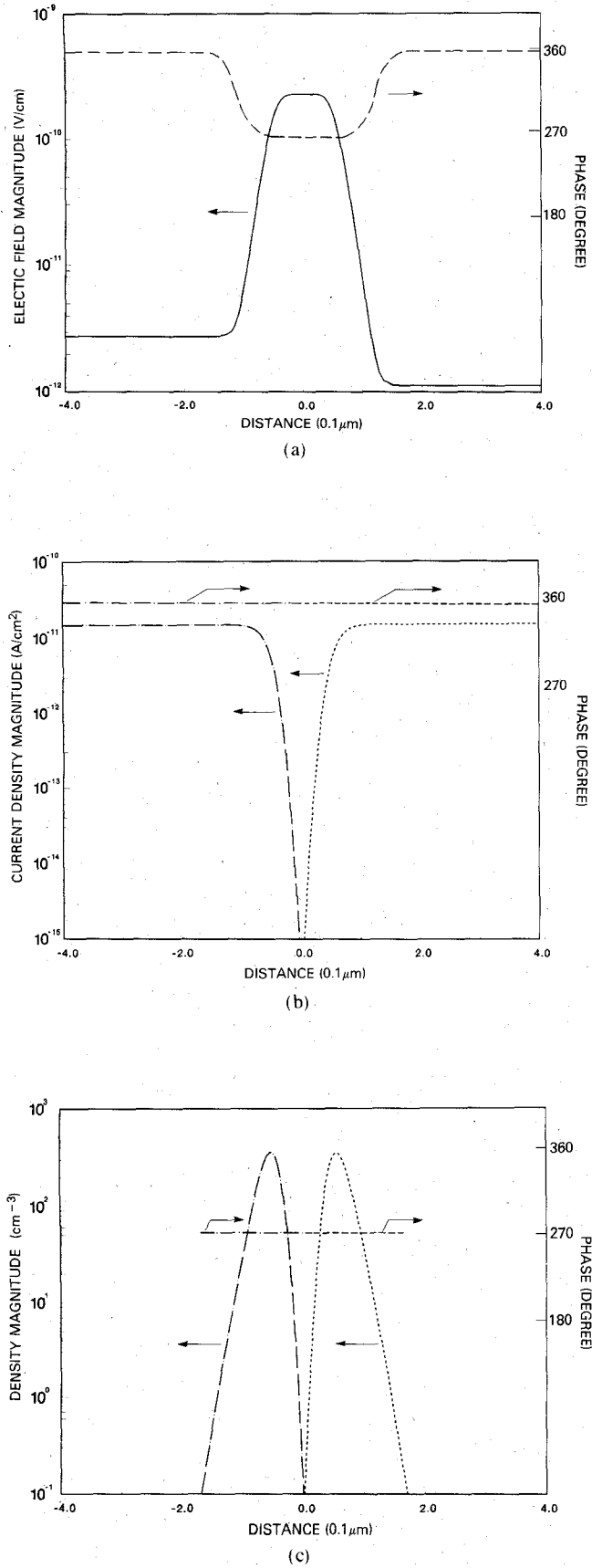


Fig. 7. Si transmission line ac magnitude and phase spatial profiles of (a) electric field  $\tilde{E}_x$ , (b) electron  $\tilde{J}_{nx}$  (—) and hole  $\tilde{J}_{px}$  (—·—) current densities, and (c) electron  $\tilde{n}$  (—) and hole  $\tilde{p}$  (—·—) densities for  $V_a = +0.3$  V and  $f = 10$  GHz. Parameters are the same as in Fig. 7.

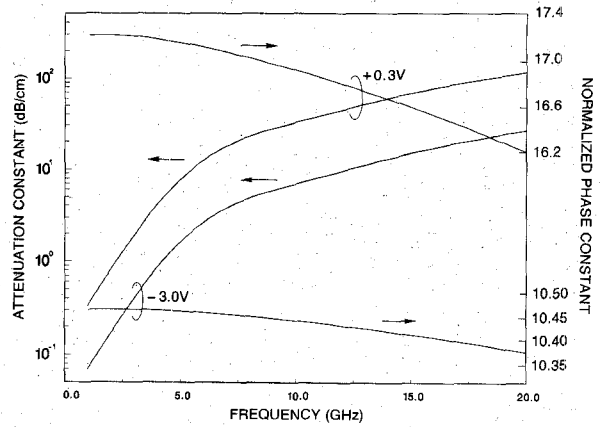


Fig. 8. Calculated normalized phase constants,  $\beta/\beta_0$ , and semiconductor attenuation constants,  $\alpha_s$  (dB/cm), for the Si transmission line containing an abrupt bipolar junction at two values of applied dc bias voltage  $V_a$ . Parameters are set at  $N_{d0} = N_{a0} = 10^{17} \text{ cm}^{-3}$ ,  $l = 3 \mu\text{m}$ , and  $T = 300 \text{ K}$ .

volume are unequal,  $J_{n0x} \approx 2.4J_{p0x}$ . A smaller discrepancy holds for the majority current densities,  $J_{n0x} \approx 1.02J_{p0x}$ . In contrast to the reverse-biased semiconductor volume situation, the forward-biased  $V_a = +0.3$  V case shows that carrier injection is so significant that in the p area  $J_{p0x}$  exceeds  $J_{p0x} \approx 2.35J_{p0x}$ , and in the n area  $J_{p0x} \approx 0.41J_{n0x}$ . The ac simulations were run with impressed terminal currents operating at frequencies from 1 GHz to 20 GHz. Fig. 6(a)–(c) shows the magnitudes and phase angles (with respect to the terminal current) for the ac electric field  $\tilde{E}_x$ , the electron  $\tilde{J}_{nx}$  and hole  $\tilde{J}_{px}$  current densities, and the electron  $\tilde{n}$  and hole  $\tilde{p}$  carrier densities, respectively, for a dc bias of  $V_a = -3.0$  V and a frequency of 10 GHz. Fig. 6(a) and (b) demonstrates that the displacement current density,  $j\omega\epsilon\tilde{E}_x \approx -\omega\epsilon\tilde{E}_{x,\text{imag}} \approx \tilde{J}_t$ , is predominant for  $-0.14 \leq x \leq 0.14 \mu\text{m}$ , and that for  $|x| \geq 0.14 \mu\text{m}$ , the hole  $\tilde{J}_{px,\text{real}} \approx q\mu_p\tilde{E}_{x,\text{real}} \approx \tilde{J}_t$  ( $\mu_p \approx \mu_{p0}$ ) or the electron  $\tilde{J}_{nx,\text{real}} \approx q\mu_n\tilde{E}_{x,\text{real}} \approx \tilde{J}_t$  ( $\mu_n \approx \mu_{n0}$ ) particle current density predominates. Fig. 7 gives the results for a dc forward bias of  $V_a = +0.3$  V and  $f = 10$  GHz.

The complex propagation constants ( $\gamma = \alpha_s + j\beta$ ) are calculated for several ac frequencies and shown in Fig. 8. Slow wave factors,  $\beta/\beta_0$ , are found to be similar to those in the GaAs Schottky microstrip case for both forward and reverse applied bias and display a slight frequency dispersion. The Si semiconductor material loss, however, is seen to be very large. These large attenuations may be attributed to the relatively small electron and hole mobilities and to the presence of two “lossy” bulk regions which constitute 90 percent of the structure’s length, even at  $V_a = -3.0$  V reverse bias.

## V. CONCLUSION

A transport-field formulation and solution method to find the small-signal propagation constant  $\gamma$  has been presented for transmission lines over an inhomogeneously doped semiconductor substrate, under transverse dc bias. Net doping concentration  $N(x) = N_d(x) - N_a(x)$  allows for an arbitrary distribution in the  $x$  direction. Internal

junctions and severely graded areas within the semiconductor volume may be treated besides more slowly varying distributions. The transport model includes electrons and holes, recombination-generation processes, dc and ac field-dependent mobilities and diffusion constants, and boundary condition contact effects. The dispersion of the propagating wave due to doping inhomogeneity, substrate loss, and other transport effects is accounted for by the self-consistent approach used here. The dominant  $\text{TM}_z$  mode method should be applicable for strip widths  $w \gtrsim l$  = transverse semiconductor thickness, and millimeter-wave frequencies based upon a maximum transport model frequency limit inversely proportional to the energy relaxation time [30]. For GaAs, this limit is 50–100 GHz, depending upon the maximum dc electric field.

Two layered structures of interest to monolithic microwave integrated circuits and high-speed digital integrated circuits were studied. The first structure, a GaAs voltage variable phase shifter, is representative of applications found in monolithic microwave integrated circuits. The second structure, a transmission line over a Si bipolar junction, is representative of applications found in high-speed digital integrated circuits. Both structures addressed the problem of present interest, i.e., the modification of propagation characteristics due to altered transport conditions caused by the applied dc bias. This problem is of special interest where interconnections pass into regions near or over active devices.

The solution method calculated the dc carrier densities, quasi-Fermi potentials, dc electric potential, and dc electric field in order to find the correct ac carrier densities, electric field, and current densities. The propagation constant  $\gamma$  was then determined from the ac information for both structures. Detailed transport variable information, as provided by the solution method, allows insight to be gained about the location of ac and dc carriers, the relative contributions of particle and displacement currents to the total ac current, and other valuable facts. This transport variable information provides insight into how the transport affects the calculation of  $\gamma$ . For example, the redistribution of carriers in the vicinity of junctions such as the Schottky barrier in the GaAs phase shifter structure is shown to influence the propagation constant. Specifically, the  $\gamma$  result shows that a simplified full-wave field solver, without the more detailed physical transport processes provided in our model, overestimates the wave slowing. Good agreement with experimental data is obtained for that particular example when  $f > 10$  GHz and  $V_a = 0.5$  V.

## APPENDIX I

If  $z$ -component currents are retained (except  $J_{z0} = 0$ ), then

$$\begin{aligned} \frac{d^2\tilde{E}_x}{dx^2} + \gamma^2\tilde{E}_x - \frac{q}{\epsilon} \frac{d}{dx}(\tilde{p} - \tilde{n}) \\ = -\omega^2\mu\epsilon\tilde{E}_x + j\omega\mu(\tilde{J}_{nx} + \tilde{J}_{px}) \end{aligned} \quad (\text{A1a})$$

$$\begin{aligned} \frac{d^2\tilde{E}_z}{dx^2} + \gamma^2\tilde{E}_z + \gamma \frac{q}{\epsilon}(\tilde{p} - \tilde{n}) \\ = -\omega^2\mu\epsilon\tilde{E}_z + j\omega\mu(\tilde{J}_{nz} + \tilde{J}_{pz}) \end{aligned} \quad (\text{A1b})$$

$$\frac{d\tilde{J}_{nx}}{dx} - \gamma\tilde{J}_{nz} = j\omega q\tilde{n} + qR_{ac}(\tilde{n}, \tilde{p}; n_0, p_0) \quad (\text{A1c})$$

$$\frac{d\tilde{J}_{px}}{dx} - \gamma\tilde{J}_{pz} = -j\omega q\tilde{p} - qR_{ac}(\tilde{n}, \tilde{p}; n_0, p_0) \quad (\text{A1d})$$

$$\begin{aligned} \tilde{J}_{nx} = q[\mu_{naz}(E_{x0})n_0\tilde{E}_x + \mu_n(E_{x0})E_{x0}\tilde{n}] \\ + qD_n(E_{x0}) \frac{d\tilde{n}}{dx} \end{aligned} \quad (\text{A1e})$$

$$\tilde{J}_{nz} = q\mu_{naz}(E_{x0})n_0\tilde{E}_z - qD_n(E_{x0})\gamma\tilde{n} \quad (\text{A1f})$$

$$\begin{aligned} \tilde{J}_{px} = q[\mu_{paz}(E_{x0})p_0\tilde{E}_x + \mu_p(E_{x0})E_{x0}\tilde{p}] \\ - qD_p(E_{x0}) \frac{d\tilde{p}}{dx} \end{aligned} \quad (\text{A1g})$$

$$\tilde{J}_{pz} = q\mu_{paz}(E_{x0})p_0\tilde{E}_z + qD_p(E_{x0})\gamma\tilde{p}. \quad (\text{A1h})$$

Equations (6) must be solved first, subject to appropriate BC's, in order to provide the dc values required in (A1) which vary spatially. By Faraday's law,

$$\tilde{H}_z = \frac{1}{j\omega\mu} \left[ \frac{\partial\tilde{E}_x}{\partial y} - \frac{\partial\tilde{E}_y}{\partial x} \right] = 0. \quad (\text{A2})$$

Therefore the propagating wave is a  $\text{TM}_z$  mode. Thus

$$\tilde{E}_x = \frac{1}{\gamma^2 + k^2} \left[ j\omega\mu\tilde{J}_x - \gamma \frac{d\tilde{E}_z}{dx} \right] \quad (\text{A3a})$$

$$\tilde{H}_y = \frac{1}{j\omega\mu} \left[ \gamma\tilde{E}_x + \frac{d\tilde{E}_z}{dx} \right]. \quad (\text{A3b})$$

Here  $k^2 = \omega^2\epsilon\mu$ . Dropping (A1a) from (A1) and employing (A3a) allows a coupled set of nonlinear, ordinary differential equations to be solved for five ac variables, from which all of the other variables may be found:

$$\begin{aligned} \frac{d\xi}{dx} = [j\omega q\mu(\mu_{naz}n_0 + \mu_{paz}p_0) - \gamma^2 - k^2]\tilde{E}_z \\ + \gamma \left( j\omega\mu qD_p - \frac{q}{\epsilon} \right) \tilde{p} + \gamma \left( \frac{q}{\epsilon} - j\omega\mu qD_n \right) \tilde{n} \end{aligned} \quad (\text{A4a})$$

$$\frac{d\tilde{E}_z}{dx} = \xi \quad (\text{A4b})$$

$$\frac{d\tilde{J}_{nx}}{dx} = q\mu_{naz}n_0\gamma\tilde{E}_z + q(j\omega - D_n\gamma^2)\tilde{n} + qR_{ac}(\tilde{n}, \tilde{p}; n_0, p_0) \quad (\text{A4c})$$

$$\frac{d\tilde{J}_{px}}{dx} = q\mu_{paz}p_0\gamma\tilde{E}_z + q(D_p\gamma^2 - j\omega)\tilde{p} - qR_{ac}(\tilde{n}, \tilde{p}; n_0, p_0) \quad (\text{A4d})$$

$$\begin{aligned} \frac{d\tilde{n}}{dx} &= \frac{1}{qD_n} \left[ -\frac{j\omega\mu q\mu_{max}n_0}{\gamma^2 + k^2} \right] \tilde{J}_{nx} - \frac{j\omega\mu\mu_{max}n_0}{D_n(\gamma^2 + k^2)} \tilde{J}_{px} \\ &+ \frac{\mu_{max}n_0\gamma}{D_n(\gamma^2 + k^2)} \xi - \frac{\mu_n}{D_n} E_{x0} \tilde{n} \end{aligned} \quad (A4e)$$

$$\begin{aligned} \frac{d\tilde{p}}{dx} &= \frac{1}{qD_p} \left[ \frac{j\omega\mu q\mu_{pax}p_0}{\gamma^2 + k^2} - 1 \right] \tilde{J}_{nx} + \frac{j\omega\mu\mu_{pax}p_0}{D_p(\gamma^2 + k^2)} \tilde{J}_{px} \\ &- \frac{\mu_{pax}p_0\gamma}{D_p(\gamma^2 + k^2)} \xi + \frac{\mu_p}{D_p} E_{x0} \tilde{p} \end{aligned} \quad (A4f)$$

$$\frac{d\gamma}{dx} = 0. \quad (A4g)$$

In (A4)  $\xi$  is a dummy variable eliminating the second-order spatial derivative in (A1b), and the last equation allows  $\gamma$  to be self-consistently determined to satisfy the remaining suite of equations [25]. If  $\tilde{E}_z$  and  $\nabla \cdot \tilde{E}$  are sufficiently small so that the first two field equations in (A4) can be decoupled from the remaining five, and a small differential cell examined so that  $\gamma \rightarrow 0$ , then (A4) reduce to the fundamental  $TM_z$  mode case in (7).

It is possible to include  $y$ -component ac perturbations by retaining extra equations such as (A1a), (A1e), and (A1g) containing  $\tilde{E}_y$ ,  $\tilde{J}_{ny}$  and  $\tilde{J}_{py}$  variables. Such an inclusion creates a hybrid mode because  $\tilde{E}_y \alpha \tilde{J}_{ny} \mu_n^{-1}(E_{x0})$  and  $\partial \tilde{E}_y / \partial x \neq 0$  in (A2). In general, field-dependent mobilities will not be spatially constant, as can be seen when examining the variation of  $\mu_n$  across a pn junction area. Thus  $\tilde{E}_y$  cannot be constant and TM modes are excluded.

## APPENDIX II

In order to start the dc numerical calculations, initial values for the spatially dependent variables throughout the inhomogeneous semiconductor volume are chosen for the equilibrium solution over a selected nonuniform mesh by using the analytical expressions derived from the depletion approximation for junctions. These equilibrium formulas are provided below for the normalized variables. For the unipolar n-GaAs Schottky line case, we use

$$\bar{\psi}(\bar{x}) = \begin{cases} -\bar{N}_d(\bar{x} - \bar{x}_n)^2/2 + \bar{\psi}(\bar{x}_n), & 0 \leq \bar{x} \leq \bar{x}_n \\ \bar{\psi}(\bar{x}_n), & \bar{x}_n \leq \bar{x} \leq \bar{l} \end{cases}$$

$$\bar{\psi}(\bar{x}_n) = \ln [\bar{N}_d/\bar{n}_i]; \quad \bar{x}_n = \sqrt{2\bar{\phi}_i/\bar{N}_d}$$

$$\bar{\phi}_i = \bar{\psi}(\bar{x}_n) + \bar{\phi}_B - \bar{E}_g/2$$

$$\bar{E}_{x0}(\bar{x}) = -d\bar{\psi}(\bar{x})/d\bar{x}; \quad \bar{\phi}_n(\bar{x}) = 0; \quad \bar{J}_{n0x}(\bar{x}) = 0. \quad (A5)$$

Here,  $\bar{x}_n$  and  $\bar{\phi}_i$  are the normalized depletion region depth and built-in potential.

In the bipolar Si abrupt junction case, we use

$$\bar{\psi}(\bar{x}) = \begin{cases} \bar{\psi}(-\bar{x}_p), & -l/2 \leq \bar{x} \leq -\bar{x}_p \\ \bar{\psi}(-\bar{x}_p) + \bar{N}_a(\bar{x} + \bar{x}_p)^2/2, & -\bar{x}_p \leq \bar{x} \leq 0 \\ \bar{\psi}(\bar{x}_n) - \bar{N}_d(\bar{x} - \bar{x}_n)^2/2, & 0 \leq \bar{x} \leq \bar{x}_n \\ \bar{\psi}(\bar{x}_n), & \bar{x}_n \leq \bar{x} \leq l/2 \end{cases}$$

$$\bar{\psi}(-\bar{x}_p) = -\ln(\bar{N}_a/\bar{n}_i); \quad \bar{\psi}(\bar{x}_n) = \ln(\bar{N}_d/\bar{n}_i)$$

$$\bar{x}_p = \sqrt{2\bar{\phi}_i \bar{N}_d / [\bar{N}_a(\bar{N}_a + \bar{N}_d)]}$$

$$\bar{x}_n = \sqrt{2\bar{\phi}_i \bar{N}_a / [\bar{N}_d(\bar{N}_d + \bar{N}_a)]}$$

$$\bar{\phi}_i = \ln(\bar{N}_a \bar{N}_d / \bar{n}_i^2) \quad \bar{E}_{x0}(\bar{x}) = -d\bar{\psi}(\bar{x})/d\bar{x}$$

$$\bar{\phi}_n(\bar{x}) = \bar{\phi}_p(\bar{x}) = 0 \quad \bar{J}_{n0x}(\bar{x}) = \bar{J}_{p0x}(\bar{x}) = 0. \quad (A6)$$

Here,  $\bar{x}_n$  and  $\bar{x}_p$  are the depletion region depths extending into the n and p regions, respectively, with the metallurgical junction at  $\bar{x} = 0$ . New trial values of the variables at applied bias voltage increments  $\Delta\bar{V}_a$  can be chosen:

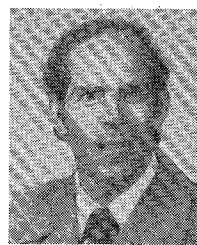
$$\begin{aligned} \bar{\psi}^T(x) &= \bar{\psi}(x) + \frac{\bar{\psi}(x) - \bar{\psi}(l)}{\bar{\psi}(0) - \bar{\psi}(l)} \Delta\bar{V}_a \\ \bar{E}_{x0}^T(x) &= \left[ 1 + \frac{\Delta\bar{V}_a}{\bar{\psi}(0) - \bar{\psi}(l)} \right] \bar{E}_{x0}(x) \\ \bar{\phi}_n^T(x) &= \bar{\psi}^T(x) - \bar{\psi}(x) + \bar{\phi}_n(x) \\ \bar{\phi}_p^T(x) &= \bar{\psi}^T(x) - \bar{\psi}(x) + \bar{\phi}_p(x) \\ \bar{J}_{n0x}^T(x) &= \bar{J}_{n0x}(x) \quad \bar{J}_{p0x}^T(x) = \bar{J}_{p0x}(x). \end{aligned} \quad (A7)$$

Notice that the second equation comes directly from the first one of (A7) using (21).

## REFERENCES

- [1] C. M. Krowne and E. J. Cukauskas, "GaAs slow wave phase shifter characteristics at cryogenic temperatures," *IEEE Trans. Electron Devices*, vol. ED-34, pp. 1183–1186, May 1987.
- [2] V. M. Hietala, Y. R. Kwon, and K. S. Champlin, "Broadband continuously variable microwave phase shifter employing a distributed schottky contact on silicon," *Electron. Lett.*, vol. 23, pp. 675–677, June 1987.
- [3] K. Fricke and H. L. Hartnagel, "GaAs MESFET optimization and new device applications based on wave property studies," in *IEEE MTT-S Int. Microwave Symp. Dig.*, June 1985, pp. 192–195.
- [4] Y. Fukuoka and T. Itoh, "Field analysis of a millimeter-wave GaAs double-drift Impatt diode in the traveling-wave mode," *IEEE Trans. Microwave Theory Tech.*, vol. MTT-33, pp. 216–220, Mar. 1985.
- [5] H. Hasegawa, M. Furukawa, and H. Yanai, "Properties of microstrip line on Si-SiO<sub>2</sub> system," *IEEE Trans. Microwave Theory Tech.*, vol. MTT-19, pp. 869–881, Nov. 1971.
- [6] C. M. Krowne, "Slow-wave propagation in two types of cylindrical waveguides loaded with a semiconductor," *IEEE Trans. Microwave Theory Tech.*, vol. MTT-33, pp. 335–339, Apr. 1985.
- [7] W. McKenzie, D. M. Barry, C. M. Snowden, and M. J. Howes, "Computer-aided design of MMIC structures," *Proc. Inst. Elec. Eng.*, vol. 133, pt. H, pp. 405–410, Oct. 1986.
- [8] T. -S. Mu, H. Ogawa, and T. Itoh, "Characteristics of multiconductor, asymmetric, slow-wave microstrip transmission lines," *IEEE Trans. Microwave Theory Tech.*, vol. MTT-34, pp. 1471–1477, Dec. 1986.
- [9] W. Heinrich and H. L. Hartnagel, "Wave-theoretical analysis of signal propagation on FET electrodes," *Electron. Lett.*, vol. 19, pp. 65–67, Jan. 1983.
- [10] M. Kurata, *Numerical Analysis for Semiconductor Devices*. Lexington, MA: Lexington Books, 1982.

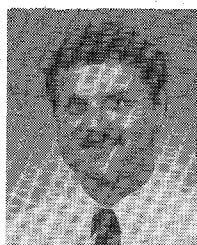
- [11] S. M. Sze, *Physics of Semiconductor Devices*, 2nd ed. New York: Wiley, 1981.
- [12] C. M. Krowne, "Perturbational solutions of the Boltzmann transport equation for  $n^+mn^+$  structures," *Proc. Inst. Elec. Eng.*, vol. 134, pt. I, pp. 93-100, June 1987.
- [13] S. Selberherr, *Analysis and Simulation of Semiconductor Devices*. New York: Springer-Verlag, 1984.
- [14] W. L. Engl, H. K. Dirks, and B. Meinerzhagen, "Device modeling," *Proc. IEEE*, vol. 71, pp. 10-33, Jan. 1983.
- [15] W. R. Curtice, "Direct comparison of the electron-temperature model with the particle-mesh (Monte-Carlo) model for the GaAs MESFET," *IEEE Trans. Electron Devices*, vol. ED-29, pp. 1942-1943, Dec. 1982.
- [16] D. S. Newman, D. K. Ferry, and J. R. Sites, "Measurement and simulation of GaAs FET's under electron-beam irradiation," *IEEE Trans. Electron Devices*, vol. ED-30, pp. 849-855, July 1983.
- [17] L. M. Dang and M. Konaka, "A two-dimensional computer analysis of triode-like characteristics of short-channel MOSFET's," *IEEE Trans. Electron Devices*, vol. ED-27, pp. 1533-1539, Aug. 1980.
- [18] J. G. Fossum and D. S. Lee, "A physical model for the dependence of carrier lifetime on doping density in nondegenerate silicon," *Solid-State Electron.*, vol. 25, pp. 741-747, Aug. 1982.
- [19] F. Masszi, P. -A. Tove, K. Bohlin and H. Norde, "Computer modeling and comparison of different rectifier ( $M-S$ ,  $M-S-M$ ,  $p-n-n^+$ ) diodes," *IEEE Trans. Electron Devices*, vol. ED-33, pp. 469-476, Apr. 1986.
- [20] N. D. Arora, J. R. Hauser, and D. J. Roulston, "Electron and hole mobilities in silicon as a function of concentration and temperature," *IEEE Trans. Electron Devices*, vol. ED-29, pp. 292-295, Feb. 1982.
- [21] A. DeMari, "An accurate numerical steady-state one dimensional solution of the  $p-n$  junction," *Solid-State Electron.*, vol. 11, pp. 33-58, Jan. 1968.
- [22] A. DeMari, "An accurate numerical one-dimensional solution of the  $p-n$  junction under arbitrary transient conditions," *Solid-State Electron.*, vol. 11, pp. 1021-1053, Nov. 1968.
- [23] H. K. Gummel, "A self-consistent iterative scheme for one-dimensional steady state transistor calculations," *IEEE Trans. Electron Devices*, vol. ED-11, pp. 455-465, Oct. 1964.
- [24] A. S. Grove, *Physics and Technology of Semiconductor Devices*. New York: Wiley, 1967.
- [25] V. Pereyra, "PASVA3: An adaptive finite-difference Fortran program for first order nonlinear, ordinary boundary problems," in *Codes For Boundary-Value Problems in Ordinary Differential Equations, Lecture Notes on Computer Science*, B. Childs et. al., Eds., vol. 76. Berlin: Springer-Verlag, 1979, pp. 67-88.
- [26] Subroutine DVCPR, International Mathematical and Statistical Libraries, Inc., Houston, TX, version 9.2, 1984.
- [27] C. M. Krowne and R. E. Neidert, "Solid state monolithic variable phase shifter with operation into the millimeter wave wavelength regime," *Int. J. Infrared Millimeter Waves*, vol. 7, pp. 715-728, May 1986.
- [28] A. K. Sinha, T. E. Smith, M. H. Read, and J. M. Poate, "n-GaAs Schottky diodes metallized with Ti and Pt/Ti," *Solid-State Electron.*, vol. 19, pp. 489-492, 1976.
- [29] K. C. Gupta, R. Garg, and I. J. Bahl, *Microstrip Lines and Slotlines*. Dedham, MA: Artech House, 1979.
- [30] G. B. Tait and C. M. Krowne, "Efficient transferred electron device simulation method for microwave and millimeter wave CAD applications," *Solid-State Electron.*, vol. 30, pp. 1025-1036, Oct. 1987.



**Clifford M. Krowne** (S'73-M'74-SM'84) attended the University of California, Berkeley, and received the B.S. degree in physics from the University of California, Davis, in 1970 and the M.S. and Ph.D degrees in electrical engineering from the University of California, Los Angeles, in 1972 and 1975, respectively.

In 1970, he was employed in the Microelectronics Division of Lockheed Missiles and Space Company. In 1976 he joined the technical staff of the Watkins-Johnson Company in Palo Alto, CA, and in 1978 he became a faculty member in the Department of Electrical Engineering at North Carolina State University, Raleigh. Dr. Krowne was a 1980 ASEE Summer Faculty Fellow at the NASA Johnson Space Center, Houston, TX. Since 1982, he has been with the Electronics Science and Technology Division of the Naval Research Laboratory, Washington, DC, studying microwave and millimeter-wave properties of active and passive solid-state devices. He is also an Adjunct Professor of Electrical Engineering, University of Maryland, College Park, MD.

Dr. Krowne has published technical papers on solid-state electronics, microwave circuits, electromagnetics, engineering education, and applied physics. He has served on the technical program conference committees of the Antennas and Propagation Society and the Microwave Theory and Techniques Society and has chaired sessions in the electromagnetic theory, microstrip antenna, and solid-state devices/circuits areas. Dr. Krowne was a member of the 1987 MTT Symposium steering committee. He is a member of Phi Kappa Phi, Tau Beta Pi, and the American Physical Society.



**Gregory B. Tait** (S'88) received the B.A. degree in physics from Amherst College, Amherst, MA, in 1982 and the M.S. degree in electrical engineering from the University of Maryland, College Park, in 1984. He is presently working toward the Ph.D. degree in electrical engineering at The Johns Hopkins University, Baltimore, MD.

From 1982 to 1985, he was employed by the Fairchild Communications and Electronics Company in Germantown, MD. Since 1986, he has been with the Electronics Science and Technology Division of the Naval Research Laboratory, Washington, DC, where his research interest include semiconductor device physics and device modeling.

Mr. Tait is a member of Phi Beta Kappa and the American Physical Society.